Understanding structural incorporation of oxygen vacancies in perovskite cobaltite films and potential consequences for electrocatalysis

Lei Jin^{a,†,*}, Feng Zhang^{b,†}, Felix Gunkel^c, Xian-Kui Wei^a, Yanxing Zhang^d, Dawei Wang^{b,*}, Juri Barthel^{a,e}, Rafal E. Dunin-Borkowski^{a,f}, and Chun-Lin Jia^{a,b}

^aErnst Ruska-Centre for Microscopy and Spectroscopy with Electrons (ER-C), Forschungszentrum Jülich GmbH, 52425 Jülich, Germany

^bSchool of Microelectronics and State Key Laboratory for Mechanical Behavior of Materials, Xi'an Jiaotong University, Xi'an 710049, China

^cPeter Grünberg Institute (PGI-7), Forschungszentrum Jülich GmbH, 52425 Jülich, Germany

^dSchool of Physics, Henan Normal University, Xinxiang 453007, China

^eCentral Facility for Electron Microscopy, RWTH Aachen University, 52074 Aachen, Germany

^fPeter Grünberg Institute (PGI-5), Forschungszentrum Jülich GmbH, 52425 Jülich, Germany

[†]L.J. and F.Z. contributed equally to this work.

^{*}Email: l.jin@fz-juelich.de (L.J.)

^{*}Email: dawei.wang@xjtu.edu.cn (D.W.)

Abstract: Owing to their excellent mixed-ionic and electronic conductivity, fast oxygen kinetics and cost efficiency, layered oxygen-deficient perovskite oxides hold great potential as highly-efficient cathodes for solid oxide fuel cells and anodes for water oxidation. Under working conditions, cation ordering is believed to substantially enhance oxygen diffusion while maintaining structural stability owing to the formation of double perovskite (DP), thus attracting extensive research attention. In contrast, the incorporation of oxygen vacancies and the associated vacancy ordering have rarely been studied at the atomic scale, despite their decisive roles in regulating the electronic and spin structures as well as in differentiating the crystal structure from DP. Here, atomicresolution transmission electron microscopy is used to directly image oxygen vacancies and measure their concentration in (Pr,Ba)CoO_{3-δ} films grown on SrTiO₃ substrates. We find that accompanied with the presence of oxygen vacancy ordering at Co-O planes, the A-O (A = Pr/Ba) planes also exhibit a breathing-like lattice modulation. Specifically, as confirmed by first-principle calculations, the AO-AO interplanar spacings are found to be linearly correlated with the vacancy concentration in the enclosing Co-O planes. On this basis, potential consequences of oxygen occupancy for the catalytic properties of structurally pure PBCO phases are discussed. Through establishing a simple correlation of oxygen concentration with the easily achievable lattice measurement, our results pave a way for better understanding the structure-performance relationship of oxygen-deficient complex cobaltites used for electrocatalysis.

INTRODUCTION

Electrochemical water splitting ($H_2O \rightarrow H_2 + \frac{1}{2}O_2$) is widely considered as one of the most attractive technologies for sustainable energy conversion and storage, such as hydrogen production, regenerative fuel cells, and rechargeable metal-air batteries [1-3]. Oxygen evolution reaction (OER) [3-6], an essential oxidative half reaction of water splitting, however, suffers from sluggish kinetics as a result of the complex four-electron oxidation process. Although precious-metal oxides, such as RuO_2 and IrO_2 [7] are widely used for electrocatalysis in order to improve the OER, their scarcity and unacceptable cost have severely hindered the industrial application.

Comparing to precious-metal oxides, layered oxygen-deficient perovskite oxides (ABO_{3-δ}, where A is a rare earth or alkaline earth metal ion and B is a transition metal (TM) ion, δ represents the vacancy concentration) are found to exhibit superior OER activity together with cost efficiency [7-15]. It has been reported that, through A-site and B-site co-doping, $Ba_{0.5}Sr_{0.5}Co_{0.8}Fe_{0.2}O_{3-\delta}$ (BSCFO) with $e_{\rm g}$ occupancy close to unity can catalyze the OER with intrinsic activity that is about one order of magnitude higher than that of the state-ofthe-art IrO₂ catalyst [7]. This is identified as a landmark in the field of perovskite catalysis; however, the drawback that its surface structure readily becomes amorphous during OER deteriorates its long-term stability [7]. This stimulates development of new strategies, such as surface treatment [8,9,16], nanostructure engineering [10], cation substitution [11,12,17] and construction of cation ordering (thus converting perovskite into double perovskite (DP)) [18-24], to improve both catalytic activity and durability. For example, by means of A-site cation order engineering, recent studies show that DPs, such as PrBaCo₂O_{6-δ} [18-22], can achieve comparable performance with that of BSCFO while maintaining more stable structures under working conditions. Different from the $e_{\rm g}$ occupancy mechanism [7], the highly efficient OER activity is attributed to a moderate O p-band centre position with respect to the Fermi level [18], which offers another approach to optimize the OER performance.

In comparison with cation ordering (thus DP structuring), the role of oxygen vacancies in the OER has been less understood particularly at the atomic scale. Recent studies [13-15,19,22] have reported that their incorporation can regulate the electronic structures and/or spin states of electrocatalysts by lowering carrier density and thus conductivity for p-type oxides [25] and by modifying the coordination numbers of TM atoms [14], *etc*. The coordination change can greatly increase the active sites and facilitate the adsorption process [14]. Meanwhile, theoretical studies predicted that electrons next to oxygen vacancies would become delocalized, which can enhance electron transport from reaction interfaces to electrodes [26,27]. In contrast, it was also found that largely increasing the concentration of oxygen vacancies in double perovskite $PrBaCo_2O_{6-\delta}$ can significantly reduce the intrinsic OER activity, owing to an excessive reduction in the elemental valence state and a high-to-low spin state transition of the TM ions [22]. Therefore, the ability of direct imaging of oxygen vacancies and further evaluation of their local concentration is essential for a comprehensive understanding of the relationship between microstructures and electrocatalytic performance.

The incorporation of oxygen vacancies often leads to the formation of oxygen vacancy ordering, as typically observed in the so-called brownmillerite-structured oxides [28]. Structurally, brownmillerite can be treated as a derivative of perovskite structure. A representative example is $SrCoO_{2.5}$ (here $\delta=0.5$), in which oxygen vacancies are aligned at every second Co-O planes, *i.e.* with stacking of ...-SrO-CoO₂-SrO-CoO_{2(1- δ)-... [28]. Accompanied with oxygen vacancy ordering, the SrO-SrO interplanar distance also exhibits a lattice modulation, which results in the cell doubling along the ordering direction and the appearance of $\frac{1}{2}\{00l\}$ (l= odd) superstructural reflections (using pseudo-cubic perovskite notations) in both x-ray and electron diffraction. The same phenomenon has been observed in our reported $Pr_{0.5}Ba_{0.5}CoO_3$ (nominal formula) films [29], where A-site cation ordering is not detected. Nevertheless, these films show comparable electrocatalytic activities to that of DP PrBaCo₂O_{6- δ} [29]. It should be noted that in literature [e.g., 18,21,22] the superstructural reflections at $\frac{1}{2}\{00l\}$ were considered as a key and even unique proof in the identification of PrBaCo₂O_{6- δ} DP structures resulted from cation ordering. Consequently, atomic-scale understanding of oxygen}

vacancy ordering in the real space is also of great importance in differentiating oxygen vacancy ordered perovskite from cation ordered DP, so that the essential electrocatalytic performance can be truly studied.

In addition, the presence of oxygen vacancy ordering (at TM-O planes) is expected to induce bright-dark stripe contrast modulations in the high-angle annular dark-field (HAADF) scanning transmission electron microscopy (STEM) images [28-33]. However, the origin of this contrast is still under debate, for example, in Co-based electrocatalytic perovskite materials such as La_{1-m}Sr_mCoO_{3-δ} (LSCO) [28,30-35]. Besides oxygen vacancy ordering, an alternative interpretation is on the basis of Co spin state ordering [34,35], which was predicted using *ab initio* calculations. As a consequence, the origin of the bright-dark stripe contrast as well as the nature of spin state and/or magnetic ordering found in these materials remains to be clarified unless the atomic details including oxygen atoms/vacancies are determined.

In the present work, experimental evidence of the incorporation of oxygen vacancies to the epitaxially grown $Pr_{0.5}Ba_{0.5}CoO_{3-\delta}$ (PBCO) thin films on $SrTiO_3$ (STO) substrates is obtained by means of atomic-resolution transmission electron microscopy (TEM). Using negative spherical aberration (C_S) imaging (NCSI) high-resolution TEM (HRTEM) technique [36,37], oxygen columns with and without vacancies are clearly revealed. By comparing the experimental images with image simulations quantitatively, the concentration of vacancies is measured and their relationship with the modulations of the AO-AO lattice spacings is also deduced. These experimental results are further confirmed by first-principles calculations, thus serving as a basis for the theoretical modeling of the electronic structures of materials, including the $Co e_g$ electrons as well as the O p-band energy with respect to the Femi energy. Finally, potential consequence for the electrocatalytic properties of PBCO via the coupling of electronic e_g band filling and atomic structure are discussed.

METHODS

Sample preparation. Thin films of nominal Pr_{0.5}Ba_{0.5}CoO₃ with thicknesses ranging from 50 to 80 nm were grown by reflection high-energy electron diffraction (RHEED) controlled pulsed laser deposition (PLD) on STO (001) single-crystal substrates at an oxygen pressure of 0.1 Torr, a laser fluence of 3.5 J/cm² and a repetition rate of 5 Hz from a ceramic target [29]. Since STO provides an almost lattice matched substrate for PBCO growth, the in-plane lattice constant of the thin films is locked to the substrate's crystal structure (see Supplemental Figure S1). After growth the samples were cooled down to room temperature in deposition pressure. Two sample films that were grown at 850 and 950 °C, respectively, were selected for TEM study, as the occurrence of superstructural reflections in x-ray diffraction (see, e.g., Supplemental Figure S1) and HAADF STEM indicates the presence/inhomogeneity of oxygen vacancy ordering at both growth temperatures [29], which is expected to influence the overall catalytic performance. It is noted that in the PLD films the overall oxygen concentration may be influenced by the growth kinetics during synthesis at different temperature as well as the formation of planar defects. Thus, a main focus of the present work is the advance in direct imaging of oxygen and quantitative analysis of its concentration in such heterogeneous materials.

Cross-sectional TEM specimens were prepared by focused ion beam milling with Ga in an FEI Helios Nanolab 400s dual beam system. The lamellar specimens were thinned using 3 kV Ar ion milling in a Bal-Tec Res-101 system, followed by final cleaning using a focused 500 eV Ar ion beam in a Fischione Nanomill 1040 instrument, to remove the damaged layers that may have been introduced during the previous milling steps.

Transmission electron microscopy. HAADF STEM imaging was performed at 200 kV in an FEI Titan G2 80-200 ChemiSTEM microscope equipped with a high-brightness field emission gun, a C_8 corrector for the probe forming lens, and a super-X energy dispersive X-ray spectroscopic (EDXS) system. The incident electron beam convergence semi-angle was 25 mrad, while the collection semi-angle was 70-200 mrad. The severe overlap between Co $L_{2,3}$ (onset: 779 eV) and Ba $M_{4,5}$ (onset: 781 eV) edges makes the determination of the fine electronic structure of Co very challenging using electron

energy loss spectroscopy. Atomic-resolution TEM images were recorded at 300 kV using a GATAN UltraScan 1000 $2k \times 2k$ charge-couple device camera in an FEI Titan 80-300 microscope with a C_S corrector for the objective lens. The NCSI technique was applied, allowing both light and heavy atoms to be imaged with high image contrast [38]. In the present study, all experimental images are distortion corrected using the lattice parameters of the STO substrate as an internal calibration standard. The precision of determining an atomic column using NCSI is better than 6 pm, as evaluated by the standard deviation of lattice parameters in both STO and PBCO, and will not be shown individually in the following text. Details on the measurement precision can be found elsewhere [39,40]. The camera modulation transfer function was measured using the knife-edge method [41] for image quantification. Multislice NCSI image simulations were carried out using Dr. Probe software [42]. Atomic models were built and visualized using VESTA software [43] together with home-made scripts.

First-principles density functional theory (DFT) calculations. First-principles calculations were conducted using generalized gradient approximation (GGA) exchange-correlation functional Perdew-Burke-Ernzerhof (PBE) [44] as implemented in the Vienna *Ab-initio* Simulation Package (VASP) [45]. Spin-polarized DFT calculations with the GGA+U method [46] were performed with the simplified spherically averaged approach, where $U_{\rm eff}$ = 3.3 eV is applied to Co d electrons [18]. In the simulation, a cutoff energy of 520 eV and a 4×2×4 Brillouin-zone sampling grid [47] were used to ensure convergence. All of the geometric structures were fully relaxed until the forces calculated on each atom have a magnitude smaller than 0.02 eV/Å. The energy convergence criterion for the calculations was set to 10^{-4} eV.

We performed the calculations in two steps. First, we constructed the PBCO supercell by constraining its in-plane lattice parameters to the value of STO (*i.e.*, fully strained) and introducing different O occupancy ratios to the CoO_{2x} plane (x = 0.25, 0.375, 0.50, 0.625, 0.75, 1.00). Then we optimized the structures to obtain the AO-AO interplanar spacings, which are in good agreement with the experimental data. Finally, we calculated the density of states (DOS) and obtained the Co e_g orbital occupancy and the O p-band centre

with respect to the Fermi level in order to understand the electrocatalytic activities of structurally pure PBCO phases. A test calculation of the Co e_g orbital occupancy was also performed on LaCoO₃ and the result is consistent with literature [48,49]. For the DOS of PBCO, all the simulated structures were initialized to a ferromagnetic state [50].

RESULTS AND DISCUSSION

Figures 1a and 1b show atomic-resolution HAADF STEM images of the samples grown at 850 and 950 °C, respectively, recorded along the [010] direction of STO. Despite the presence of a high density of planar defects in Figure 1a, both samples exhibit intensity modulations at Co-O planes, as similarly described in LSCO, etc [30-33], resulting in the appearance of dark-stripe contrast indicated by open arrows in the marked areas HCM and MCM and the inset to Figure 1a. Here, HCM and MCM denote high and medium contrast modulation area, respectively. Such modulations can be demonstrated more clearly in the form of intensity profiles of the Pr,Ba-O (black circles) and Co-O (purple circles) planes along $[00\overline{1}]$, following the cyan (Figure 1c) and blue (Figure 1d) lines obtained from the marked areas (white rectangles) shown in Figures 1a and 1b, respectively. Here, we neglect the long-range intensity variation, e.g., shown in Figure 1c, whose formation is expected to be closely linked to the presence of high density defects. For both HCM and MCM areas, it is evidenced that the intensity variations are ordered at the neighboring Co-O planes, while at the Pr,Ba-O planes random fluctuation of intensity is seen, suggesting the absence of A-site cation (i.e., Pr and Ba) ordering. This has been demonstrated in Ref. [29] (see also EDXS in Supplemental Figure S2).

In Figure 1c, the intensity difference between adjacent Co-O planes, is found to be approximately twice larger than that in Figure 1d (see dotted lines), suggesting different atomic concentration/configuration in both areas. However, such an intensity difference could be also influenced by factors like specimen thickness or mistilt from the crystallographic Laue centre, thus can only be considered as qualitative. In Figure 1d, areas with low contrast modulation (denote LCM) at Co-O planes are also observed, indicating structural inhomogeneity in the 950 °C grown sample.

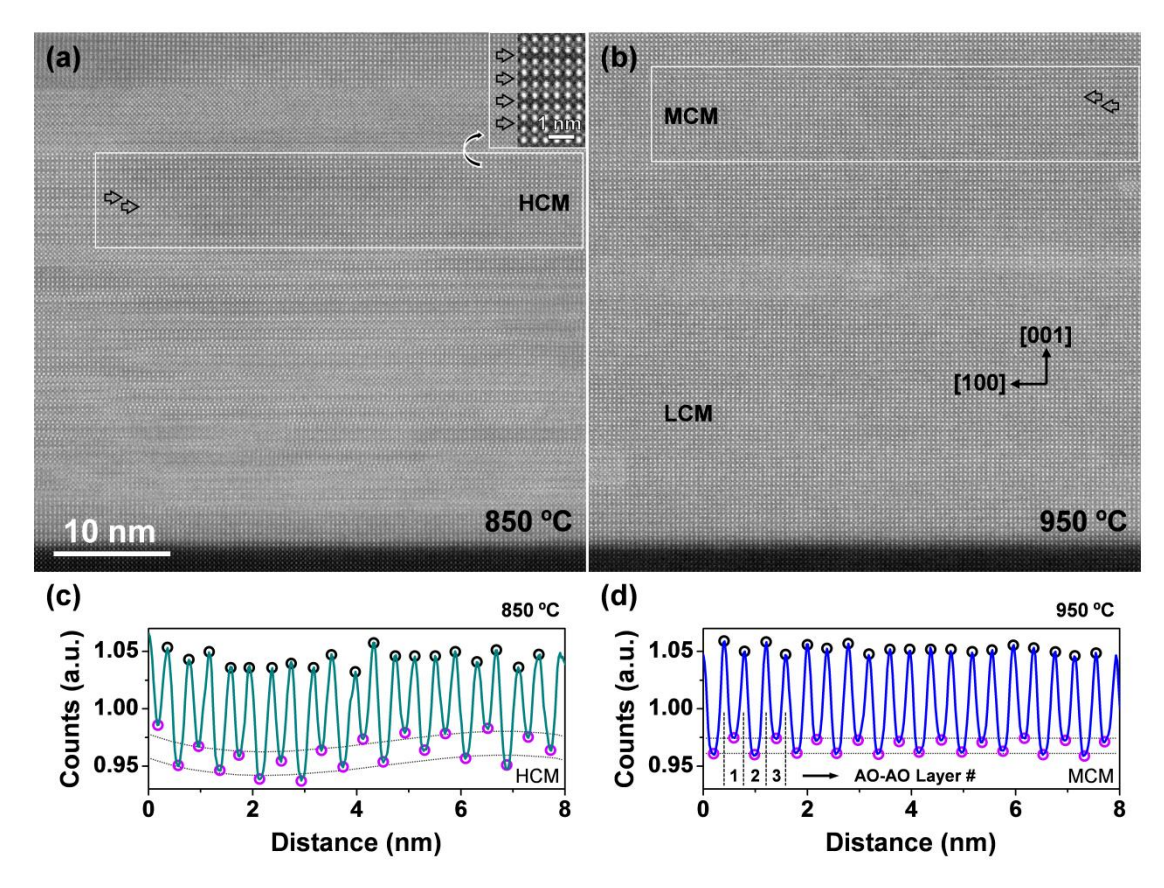


Figure 1 (a) and (b) High-angle annular dark-field scanning transmission electron microscopy images of PBCO grown at 850 and 950 °C, respectively. Inset to (a) is an average image obtained from the marked area showing the dark-stripe contrast, as indicated by open arrows. HCM, MCM, and LCM indicate high, medium, and low contrast modulation areas, respectively. (c) and (d) Intensity profiles along the [001] direction for the marked HCM and MCM areas shown in (a) and (b), respectively. The profiles are averaged (laterally) over the entire width of the marked windows. Clear intensity modulations are seen at the neighboring Co-O planes (purple dots), whereas, no modulations are detected at the Pr,Ba-O planes (black dots). The dotted lines are guide for the eye.

Since the presence of dark-stripe contrast in Co-based perovskites was reported to be accompanied with lattice variations between neighboring AO planes [30], in Figure 2 we present both in-plane and out-of-plane lattice statistics based on the unit-cell-by-unit-cell

measurement for the two marked areas in Figure 1, so that the modulations could be further assessed. It can be seen from Figures 2a and 2c that the in-plane AO-AO distance a of both areas is about 3.91 Å (standard deviation $sd \approx 0.07$ Å), suggesting that both films are fully tensile-strained ($a_{PBCO-bulk} \approx 3.86 \text{ Å}$) on the STO substrate ($a_{STO} = 3.905 \text{ Å}$). Figures 2b and 2d show the out-of-plane lattice distance c plotted as a function of AO-AO stacking layers (see Figure 1d for illustration), evidencing a breathing-like lattice modulation in both areas. Such a lattice modulation leads to larger standard deviations (\sim 0.2 Å) in Figures 2a and 2c from the mean out-of-plane lattice distance c of \sim 3.97 Å, as compared to the in-plane values. Since our analysis was performed at the areas where the cation nonstoichiometry is minor (Supplemental Figure S2), the anomalous expansion in c (under tensile strain) may be understood in term of chemical expansion [51], which usually results from the presence of oxygen vacancies. Interestingly, the calculated lattice difference between adjacent AO planes (c_{high} - c_{low} = 4.139 - 3.777 = 0.362 Å) in Figure 2b is also about twice larger than that $(c_{\text{high}} - c_{\text{low}} = 4.066 - 3.859 = 0.207 \text{ Å})$ in Figure 2c, corresponding to the observed difference in the contrast modulation in Figure 1. In Figure 2d, the breathing-like modulation could be also interrupted locally (see vertical arrow), which is most likely to be a result of the inhomogeneous structural distribution as mentioned in Figure 1b. Further examination reveals that such an ordered lattice variation is in correspondence with the Co-O intensity modulation, i.e., the AO-AO layer with large (small) c value has low (high) image intensity of Co-O plane located in between, which is also consistent with previous reports [30].

In order to clarify the origin of the dark-stripe contrast observed in the HAADF STEM images, we performed high-resolution TEM investigations under the NCSI condition and a typical result of the 850 °C grown sample is shown in Figure 3a. In this image, the viewing direction is along the pseudocubic [110] direction of PBCO and all of the three types of atomic columns, *i.e.*, (Pr,Ba)O, Co and O (see atomic model overlying the right corner; Pr,Ba: yellow; Co: blue; O: red), are imaged as bright dots on a dark background. Figure 3b shows a laterally averaged image over the entire area of Figure 3a, in which two clear differences could be seen at the adjacent Co-O planes: i) At the planes that are marked by red horizontal arrows (labeled "Ohigh"), the O columns (*e.g.*, indicated by a red

vertical arrow) exhibit higher intensities than those (*e.g.*, indicated by a green vertical arrow) located at the neighboring Co-O planes, which are marked by green horizontal arrows (labeled "O_{low}"). Such an intensity difference indicates a higher O concentration at the "O_{high}" planes. ii) The Co columns that are located at the "O_{low}" planes (*e.g.*, indicated by a white vertical arrow) also show enhanced intensities, as compared to those at the "O_{high}" planes (*e.g.*, indicated by a blue vertical arrow). This phenomenon will be discussed later.

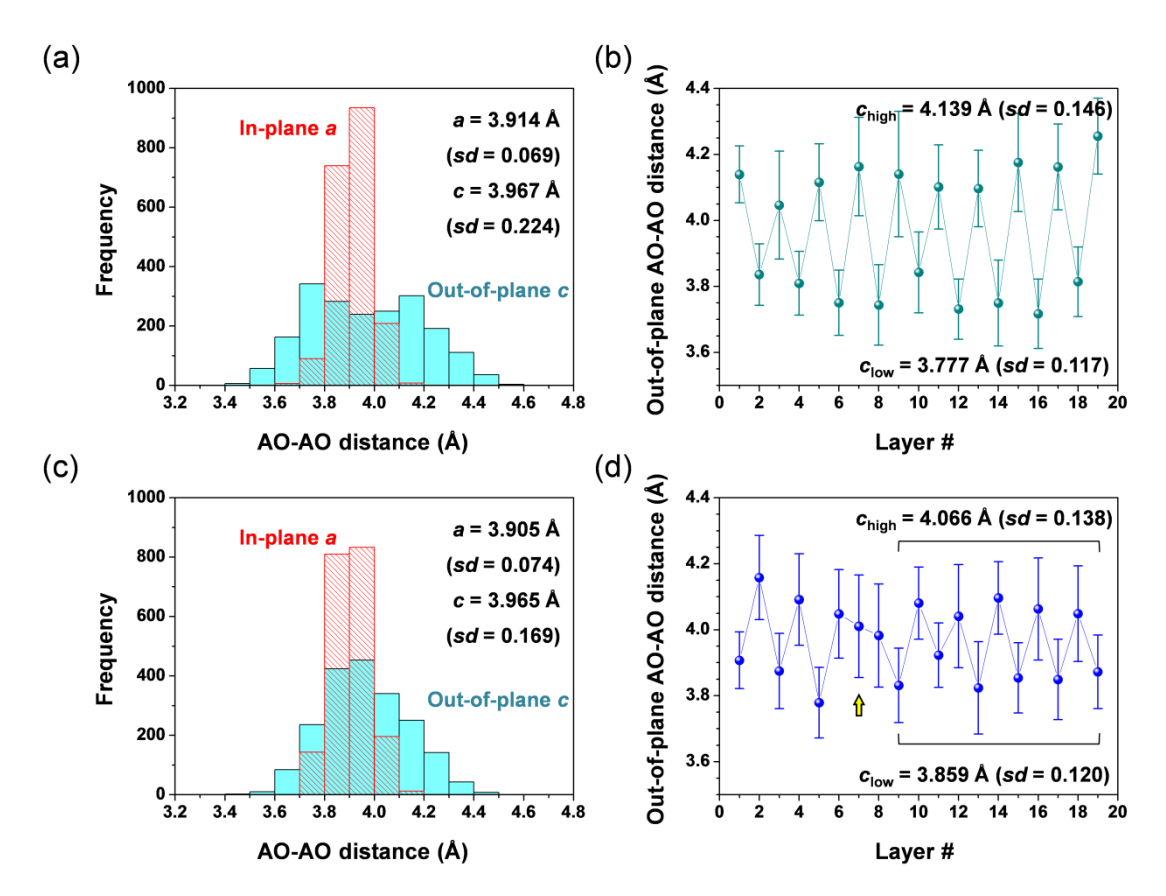


Figure 2 Lattice statistics for samples grown at (a,b) 850 and (c,d) 950 °C. (a) and (c) Histograms of the in-plane *a* and out-of-plane *c* lattice parameters, characterized in terms of the AO-AO interplanar distance. (b) and (d) Out-of-plane AO-AO interplanar distance plotted as a function of the stacking layer (see Figure 1d for schematic illustration). Breathing-like lattice modulations are evident for both samples. The marked exception in (d) is most likely to be induced by structural inhomogeneity.

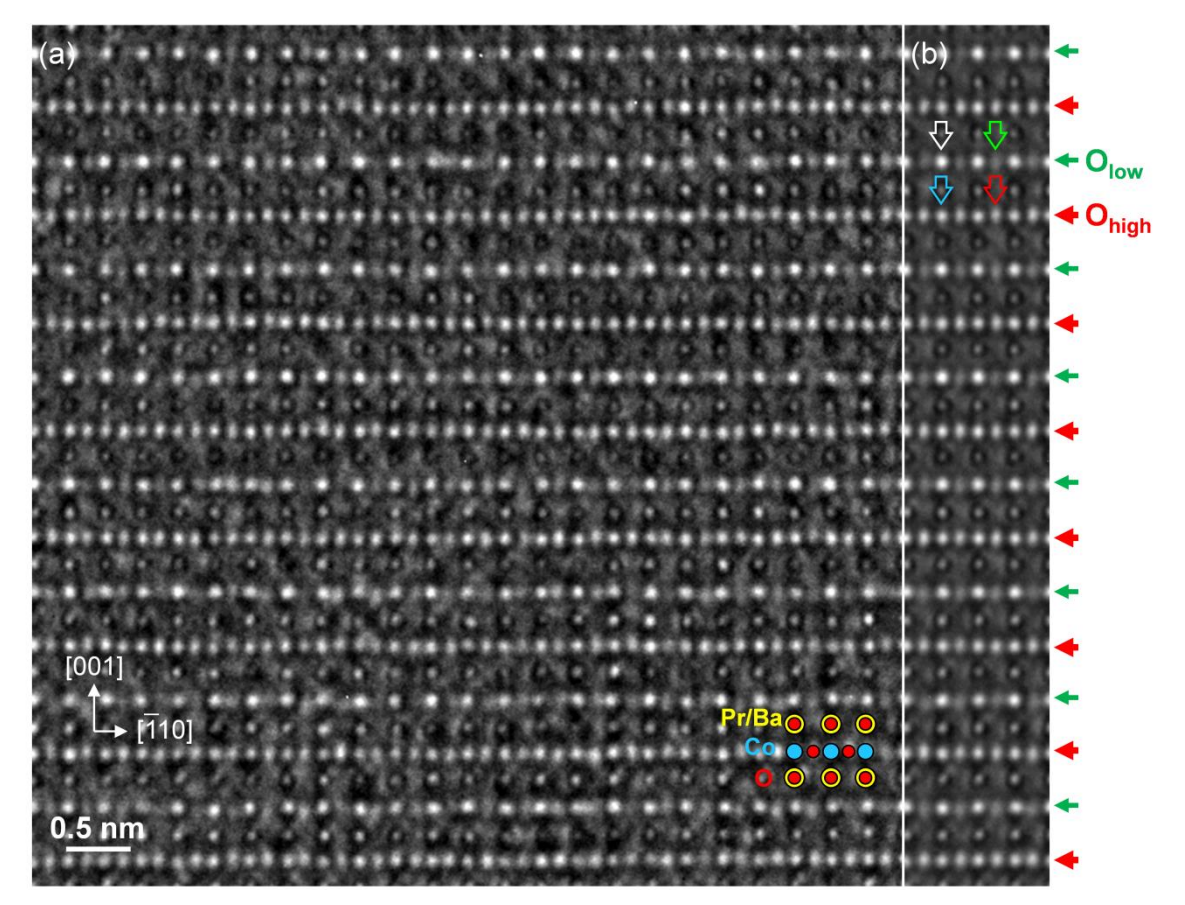


Figure 3 (a) Atomic-resolution TEM image recorded under the negative C_S imaging conditions and (b) Horizontally averaged image of (a), showing the intensity modulations of O (marked by green and red open arrows) and Co columns (marked by white and blue open arrows) at the Co-O planes (marked by horizontal arrows) in PBCO grown at 850 °C.

In order to understand the image contrast shown in Figure 3, and more importantly to evaluate the concentration of oxygen, image simulations were performed and the resulting images were compared quantitatively with experiments on the absolute contrast level [39-41,52-54] using an iterative approach. Since it is more meaningful to know the average information of oxygen content, which is expected to be highly correlated with the conductivity and band structures of PBCO and thus affects the catalytic properties, we further divided Figure 3b into 8 successive patches and obtained the mean experimental

image by averaging the intensity distribution of all of the patches, as shown in Figure 4a, for subsequent investigations. Figure 4b shows the best-fit simulated image displayed in the same grey scale as Figure 4a, using the atomic model shown in Figure 4c. Other simulation parameters are listed in Supplemental Table S1. Based on the simulation analysis, the following results are apparent:

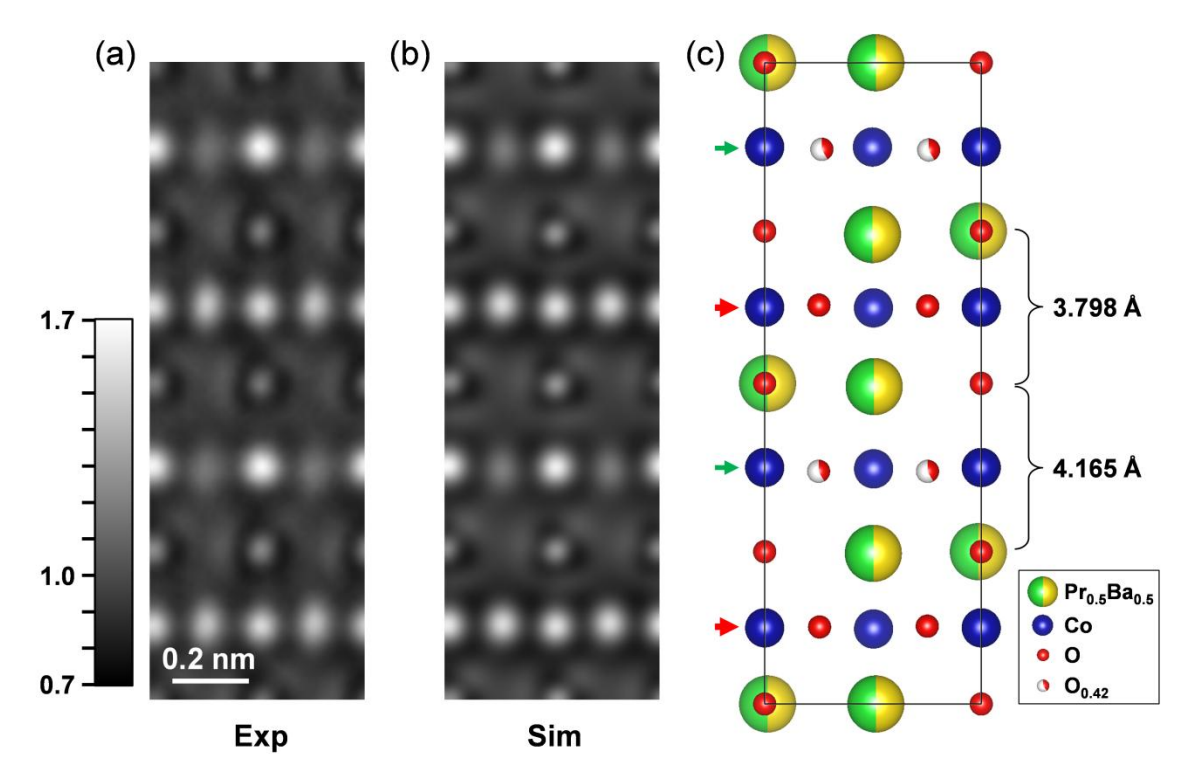


Figure 4 (a) Averaged experimental image of Figure 3 and (b) the best-fit simulated image using the atomic model shown in (c). Both images are displayed within the same absolute intensity range between 0.7 (black) and 1.7 (white). For simplicity, the atoms on each atomic column are supposed to line up coincidentally when they are viewed in the projection (see Supplemental Note 1). The stacking sequence along the pseudocubic [001] can be described as ... -Pr_{0.5}Ba_{0.5}O-CoO₂-Pr_{0.5}Ba_{0.5}O-CoO_{2×0.42}-... with a formula of Pr_{0.5}Ba_{0.5}CoO_{2.42} and lattice distance of $c_{\text{high}} + c_{\text{low}} = 7.963 \text{ Å}$.

i) The occupancy of O (*i.e.*, $x \times 100\%$) at the "O_{low}" (green arrows) and "O_{high}" (red arrows) planes is found to be approximately 42% and 100% (Figure 4c), respectively.

The occupancy difference results in the intensity modulations found at the O columns. Under the same imaging parameters used in simulation, changing the occupancy of the fully occupied O atoms to 92% yields an intensity reduction of 0.045 at these O columns. This value is marginally above the root mean square (= 0.043) of the difference image (*i.e.*, Sim - Exp), thereby, a variation of \sim 8% could be considered as a detection limit in determination of oxygen occupancy.

- ii) In simulation of Figure 4b, the reduced occupancy of O automatically leads to the intensity enhancement of the neighboring Co columns in a matched manner with respect to experiment, suggesting that the intensity modulation found at the Co columns does not relate to the intrinsic feature of the Co occupancy. This is purely an imaging effect, as the exit wave function of Co remains undisturbed by the reduced occupancy of O.
- iii) Since we do not find oxygen vacancies (within the detection limit) at the AO plane (see Supplemental Figure S3), the stacking sequence along the pseudocubic [001] direction can be described as ...-Pr_{0.5}Ba_{0.5}O-CoO₂-Pr_{0.5}Ba_{0.5}O-CoO_{2×0.42}-..., with an averaged chemical formula of Pr_{0.5}Ba_{0.5}CoO_{2.42} ($\delta = 0.58$) over the area of Figure 3a. Note that the concentration of oxygen vacancies appears to be very close to the stoichiometry for a brownmillerite phase ($\delta = 0.5$). However, its structure is found to be perovskite, in which Co atoms are still in an oxygen octahedral coordination environment. This is evidenced by the absence of Co-Co pair structures formed at the O_{low} planes, which are characteristic for the brownmillerite phase, as shown in Supplemental Figure S4.
- iv) The out-of-plane AO-AO distance (*i.e.*, c value) is determined to be 3.798 and 4.165 Å (sum: 7.963 Å) for the perovskite cells that contain " O_{high} " and " O_{low} " Co-O planes (see red and green arrows in Figure 4c), respectively, evidencing again the breathing-like modulations. The measured values are also consistent with the STEM result shown in Figure 2b.

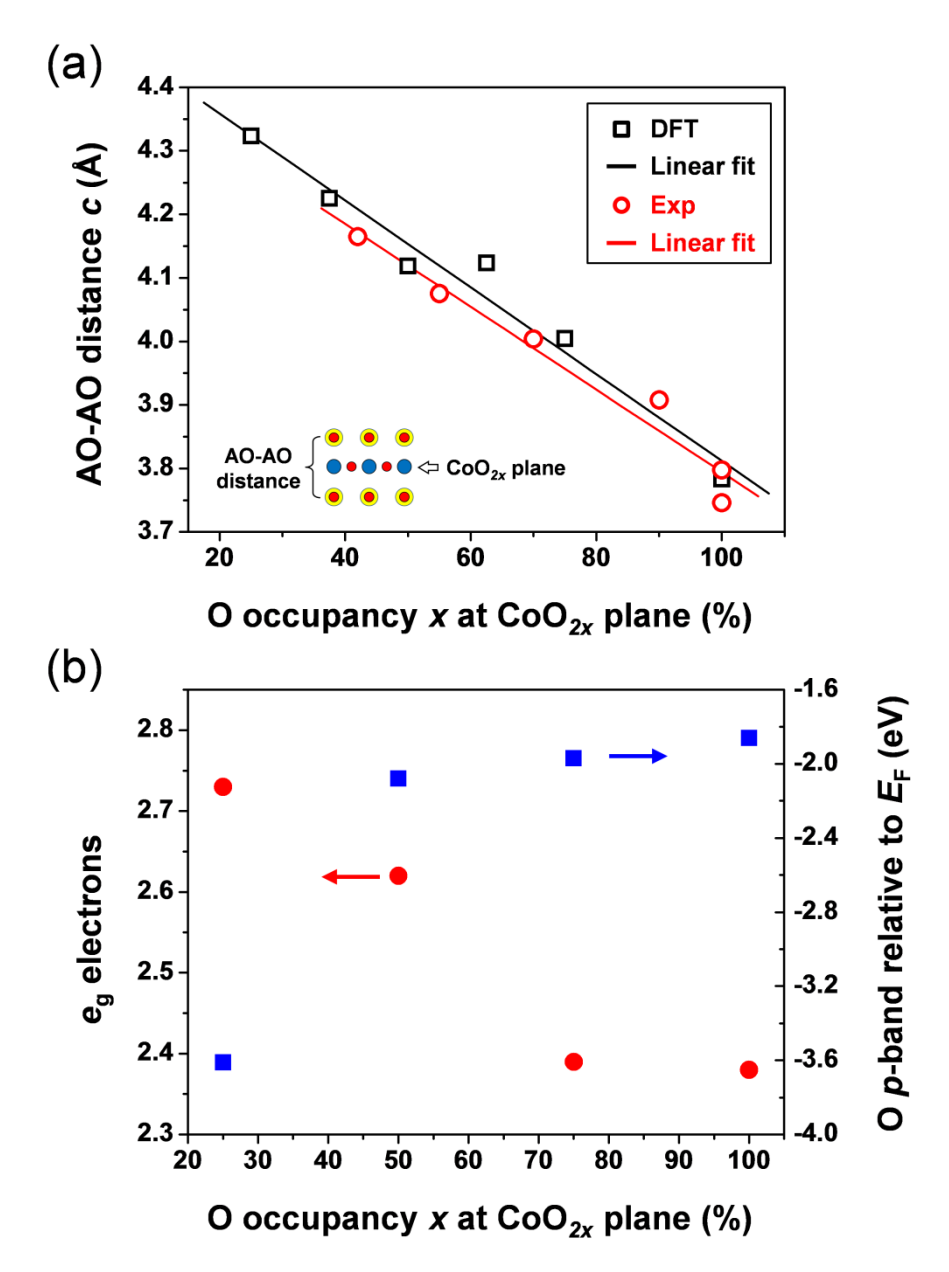


Figure 5 (a) Plot of the AO-AO interplanar distance c as a function of the oxygen site occupancy value x at the enclosing CoO_{2x} planes (see inset for schematic), showing the same linear dependence for both experimental and theoretical results. (b) Plot of Co e_g electrons and O p-band centre with respect to the Femi lever (E_F), as a function of x.

Same quantifications were also carried out on the 950 °C grown sample and the results are shown in Supplemental Figures S5 and S6, which correspond to the medium and low contrast modulation areas indicated in the HAADF STEM image (Figure 1b),

respectively. Similarly, the modulation could be described (in average) as ...- $Pr_{0.5}Ba_{0.5}O$ - $CoO_{2\times0.55}$ - $Pr_{0.5}Ba_{0.5}O$ - $CoO_{2\times0.9}$ -... (*i.e.*, $Pr_{0.5}Ba_{0.5}CoO_{2.45}$) and ...- $Pr_{0.5}Ba_{0.5}O$ - $CoO_{2\times0.7}$ - $Pr_{0.5}Ba_{0.5}O$ - CoO_{2} -... (*i.e.*, $Pr_{0.5}Ba_{0.5}CoO_{2.7}$), respectively. It is interesting to note that, although the contrast modulation in Supplemental Figure S5 appears different from that in Figure 4, the measured oxygen content and the sum of c lattice parameters (sum = 7.983 Å in Supplemental Figure S5) are approximately identical in both areas. This finding indicates different ordering degrees of oxygen vacancies and a linear correspondence between O site occupancies and c values.

First-principles density functional theory (DFT) calculations were performed to understand the correlation between O site occupancy x at CoO_{2x} planes and the interplanar c values of the corresponding AO-AO planes (see inset to Figure 5a for schematic view). After structural relaxations, we plot the calculated results of c as a function of x in Figure 5a, in combination with the measured values by quantitative HRTEM. It is clearly shown that the calculated AO-AO interplanar spacings match very well with our experimental observations, and the linear dependency of c on the O site occupancy value c is indeed evidenced. We note, similar dependence between c and c has been also reported for the oxygen deficient LSCO films [30], suggesting that such a linear relationship could be a general principle for perovskite cobaltite films.

Furthermore, we calculated the DOS of Co 3d orbitals and O p-band (Supplemental Figure S7), based on which the Co $e_{\rm g}$ electrons as well as the O p-band energy with respect to the Femi energy ($E_{\rm F}$) were obtained as a function of x. The results are shown in Figure 5b, which allows us to discuss the expected electrocatalytic properties of structurally pure PBCO phases. According to Ref. [7], the best electrocatalysis was found in materials with $e_{\rm g}$ electrons of about 1.3, and further deviation from this value leads to performance degradation. In the present case, the $e_{\rm g}$ filling increases as a general trend when the occupancy value x decreases, which indicates that introducing oxygen vacancies to PBCO may be detrimental to the electrocatalytic performance. On the other hand, the O p-band centre for stoichiometric PBCO (i.e., x = 1.0) is at -1.86 eV from $E_{\rm F}$, which might be too close to the so-called "stable/amorphized" boundary, as proposed in

Ref. [18]. Accordingly, decreasing x can effectively push the p-band centre to the lower energy position, which should be beneficial to the stability of catalysts. Therefore, a moderate concentration of oxygen occupancy, e.g., ~75%, should be highly desirable in order to achieve both high performance and high durability.

In experiment, the electrocatalytic activity of the entire PBCO film grown at different temperatures was discussed in detail revealing only a small variation of activity [29], potentially due to the overall structural inhomogeneity, hosting vacancy-ordered and disorder regions, and resulting in a similar (averaged) activity across the samples. Based on DFT, we can conclude that phase-pure ordered PBCO thin films may have the potential to provide tailored electronic structure and $e_{\rm g}$ band filling, beneficial for catalytic activity. Meanwhile, it should be noted that homogenous model catalysts need to be achieved in order to validate the abovementioned behavior, which however proofs difficult based on our quantitative electron microscopy results and thus requires further investigations.

A final remark is that in the present study we mainly compare similar strain states and minimum lattice mismatch from substrates on the structure and catalytic properties of PBCO. However, it was reported that the oxygen vacancy formation and ordering are strongly strain dependent, for example, in perovskite oxide $CaMnO_3$ (space group: Pnma, No.62; Glazer's notation: $a^*b^+c^*$) [55], indicating an additional influence parameter for the structural ordering. On the one hand, tensile strain can lower the formation energy of oxygen vacancies, consistent with the chemical expansion concept [51] that oxygen deficiency increases the molar volume in oxides. On the other hand, tensile strain can differentiate the formation energy for different oxygen lattice sites (*i.e.*, nonequivalent oxygen sites as in the Pnma system). Owing to the structural similarity between PBCO and $CaMnO_3$, it is reasonable to expect that the epitaxially tensile strain is one of the major driven forces to induce oxygen vacancy ordering. Future understanding of lattice strain on the oxygen incorporation and ordering in PBCO is thus desirable.

CONCLUSION

Using atomic-resolution TEM, the incorporation of oxygen vacancies to the epitaxially grown PBCO thin films on STO substrates is investigated quantitatively. The concentration of oxygen vacancies is quantified on the basis of NCSI technique in comparison with image simulations. A linear relationship between the concentration of oxygen vacancies and the AO-AO lattice spacing modulations are demonstrated by both experimental measurements and first-principles DFT calculations. In addition, the relationship between oxygen occupancy and expected catalytic properties is also discussed for structurally pure PBCO phases. The linear relation provides a basis for a simple and practical solution to estimate the oxygen concentration, particularly at localized regions and/or with moderate time resolution (*e.g.*, in the vicinity of the active site areas for *in situ* electrocatalysis), based on the easily achievable lattice measurements. Our research thus paves a way for further understanding the structure-performance relationship in oxygen deficient PBCO electrocatalysts and may also serve as a basis for future study of the near surface reaction during *in situ* electrocatalysis.

ASSOCIATED CONTENT

Supporting Information

The Supporting Information is available free of charge at:

XRD patterns and reciprocal space map information, atomic-resolution EDXS elemental maps, NCSI images taken from different samples and/or different orientations together with image quantifications, parameters for image simulations, Density-of-states of Co 3d orbitals and O p-bands calculated from first-principles density functional theory for different O occupancies at CoO_{2x} planes.

AUTHOR INFORMATION

Corresponding Authors

Lei Jin – Ernst Ruska-Centre for Microscopy and Spectroscopy with Electrons (ER-C), Forschungszentrum Jülich GmbH, 52425 Jülich, Germany; orcid.org/0000-0001-6924-2364; Email: l.jin@fz-juelich.de

Dawei Wang – School of Microelectronics and State Key Laboratory for Mechanical Behavior of Materials, Xi'an Jiaotong University, Xi'an 710049, China; orcid.org/0000-0002-5121-9841; Email: dawei.wang@xjtu.edu.cn

Authors

Feng Zhang – School of Microelectronics and State Key Laboratory for Mechanical Behavior of Materials, Xi'an Jiaotong University, Xi'an 710049, China; orcid.org/0000-0001-7070-6947

Felix Gunkel – Peter Grünberg Institute (PGI-7), Forschungszentrum Jülich GmbH, 52425 Jülich, Germany; orcid.org/0000-0003-1178-9986

Xian-Kui Wei – Ernst Ruska-Centre for Microscopy and Spectroscopy with Electrons (ER-C), Forschungszentrum Jülich GmbH, 52425 Jülich, Germany; orcid.org/0000-0003-4320-1120

Yanxing Zhang – School of Physics, Henan Normal University, Xinxiang 453007, China; orcid.org/0000-0002-8381-8398

Juri Barthel – Ernst Ruska-Centre for Microscopy and Spectroscopy with Electrons (ER-C), Forschungszentrum Jülich GmbH, 52425 Jülich, Germany and Central Facility for Electron Microscopy, RWTH Aachen University, 52074 Aachen, Germany; orcid.org/0000-0003-3914-4346

Rafal E. Dunin-Borkowski – Ernst Ruska-Centre for Microscopy and Spectroscopy with Electrons (ER-C), Forschungszentrum Jülich GmbH, 52425 Jülich, Germany and Peter Grünberg Institute (PGI-5), Forschungszentrum Jülich GmbH, 52425 Jülich, Germany; orcid.org/0000-0001-8082-0647

Chun-Lin Jia – Ernst Ruska-Centre for Microscopy and Spectroscopy with Electrons (ER-C), Forschungszentrum Jülich GmbH, 52425 Jülich, Germany and School of Microelectronics and State Key Laboratory for Mechanical Behavior of Materials, Xi'an Jiaotong University, Xi'an 710049, China; orcid.org/0000-0001-7536-9521

Author Contributions

L.J. and F.Z. contributed equally to this work.

Notes

The authors declare no competing financial interest.

ACKNOWLEDGMENTS

The authors thank Doris Meertens and Yan Lu for FIB preparation of specimens for TEM investigations. F.Z and D.W. acknowledge the support of National Natural Science Foundation of China, Grant No. 11974268.

REFERENCES

- (1) Roger, I.; Shipman, M. A.; Symes, M. D. Earth-abundant catalysts for electrochemical and photoelectrochemical water splitting. *Nat. Rev. Chem.* **2017**, *1*, 0003.
- (2) McHugh, P. J.; Stergiou, A. D.; Symes, M. D. Decoupled electrochemical water splitting: From fundamentals to applications. *Adv. Energy. Mater.* **2020**, *10*, 2002453.
- (3) Yu, M.; Budiyanto, E.; Tüysüz, H. Principles of water electrolysis and recent progress in cobalt-, nickel-, and iron-based oxides for the oxygen evolution reaction. *Angew. Chem. Int. Ed.* **2022**, *61*, e202103824.
- (4) Tahir, M.; Pan, L.; Idrees, F.; Zhang, X.; Wang, L.; Zou, J. J.; Wang, Z. L. Electrocatalytic oxygen evolution reaction for energy conversion and storage: A comprehensive review. *Nano Energy* **2017**, *37*, 136-157.
- (5) Liu, J.; Liu, H.; Chen, H.; Du, X.; Zhang, B.; Hong, Z.; Sun, S.; Wang, W. Progress and challenges toward the rational design of oxygen electrocatalysts based on a descriptor approach. *Adv. Sci.* **2020**, *7*, 1901614.

- (6) Song, J.; Wei, C.; Huang, Z. F.; Liu, C.; Zeng, L.; Wang, X.; Xu, Z. J. A review on fundamentals for designing oxygen evolution electrocatalysts. *Chem. Soc. Rev.* **2020**, *49*, 2196-2214.
- (7) Suntivich, J.; May, K. J.; Gasteiger, H. A.; Goodenough, J. B.; Shao-Horn, Y. A perovskite oxide optimized for oxygen evolution catalysis from molecular orbital principles. *Science* **2011**, *334*, 1383-1385.
- (8) Jung, J. I.; Jeong, H. Y.; Kim, M. G.; Nam, G.; Park, J.; Cho, J. Fabrication of Ba_{0.5}Sr_{0.5}Co_{0.8}Fe_{0.2}O_{3-δ} catalysts with enhanced electrochemical performance by removing an inherent heterogeneous surface film layer. *Adv. Mater.* **2015**, *27*, 266-271.
- (9) Guo, Y.; Tong, Y.; Chen, P.; Xu, K.; Zhao, J.; Lin, Y.; Chu, W.; Peng, Z.; Wu, C.; Xie, Y. Engineering the electronic state of a perovskite electrocatalyst for synergistically enhanced oxygen evolution reaction. *Adv. Mater.* **2015**, *27*, 5989-5994.
- (10) Zhou, S.; Miao, X.; Zhao, X.; Ma, C.; Qiu, Y.; Hu, Z.; Zhao, J.; Shi, L.; Zeng, J. Engineering electrocatalytic activity in nanosized perovskite cobaltite through surface spin-state transition. *Nat. Commun.* **2016**, *7*, 11510.
- (11) Zhu, Y.; Zhou, W.; Chen, Z. G.; Chen, Y.; Su, C.; Tadé, M. O.; Shao, Z. SrNb_{0.1}Co_{0.7}Fe_{0.2}O_{3-δ} perovskite as a next-generation electrocatalysts for oxygen evolution in alkaline solution. *Angew. Chem. Int. Ed.* **2015**, *54*, 3897-3901.
- (12) Xu, X.; Su, C.; Zhou, W.; Zhu, Y.; Chen, Y.; Shao, Z. Co-doping strategy for developing perovskite oxides as highly efficient electrocatalysts for oxygen evolution reaction. *Adv. Sci.* **2016**, *3*, 1500187.
- (13) Petrie, J. R.; Jeen, H.; Barron, S. C.; Meyer, T. L.; Lee, H. N. Enhancing perovskite electrocatalysis through strain tuning of the oxygen deficiency. *J. Am. Chem. Soc.* **2016**, *138*, 7252-7255.
- (14) Kim, J.; Yin, X.; Tsao, K. C.; Fang, S.; Yang, H. Ca₂Mn₂O₅ as oxygen-deficient perovskite electrocatalyst for oxygen evolution reaction. *J. Am. Chem. Soc.* **2014**, *136*, 14646-14649.
- (15) Pan, Y.; Xu, X.; Zhong, Y.; Ge, L.; Chen, Y.; Veder, J. P. M.; Guan, D.; O'Hayre, R.; Li, M.; Wang, G.; Wang, H.; Zhou, W.; Shao, Z. Direct evidence of

- boosted oxygen evolution over perovskite by enhanced lattice oxygen participation. *Nat. Commun.* **2020**, *11*, 2002.
- (16) Baeumer, C.; Li, J.; Lu, Q.; Liang, A. Y. L.; Jin, L.; Martins, H. P.; Duchoň, T.; Glöß, M.; Gericke, S. M.; Wohlgemuth, M. A.; Giesen, M.; Penn, E. E.; Dittmann, R.; Gunkel, F.; Waser, R.; Bajdich, M.; Nemšák, S.; Mefford, J. T.; Chueh, W. C. Tuning electrochemically driven surface transformation in atomically flat LaNiO₃ thin films for enhanced water electrolysis. *Nat. Mater.* **2021**, *20*, 674-682.
- (17) Weber, M. L.; Baeumer, C.; Mueller, D. N.; Jin, L.; Jia, C. L.; Bick, D. S.; Waser, R.; Dittmann, R.; Valov, I.; Gunkel, F. Electrolysis of water at atomically tailored epitaxial cobaltite surfaces. *Chem. Mater.* **2019**, *31*, 2337-2346.
- (18) Grimaud, A.; May, K. J.; Carlton, C. E.; Lee, Y. L.; Risch, M.; Hong, W. T.; Zhou, J.; Shao-Horn, Y. Double perovskites as a family of highly active catalysts for oxygen evolution in alkaline solution. *Nat. Commun.* **2013**, *4*, 2439.
- (19) Enriquez, E.; Xu, X.; Bao, S.; Harrell, Z.; Chen, C.; Choi, S.; Jun, A.; Kim, G.; Whangbo, M. H. Catalytic dynamics and oxygen diffusion in doped PrBaCo₂O_{5.5+δ} thin films. *ACS Appl. Mater. Interfaces* **2015**, *7*, 24353-24359.
- (20) Bick, D. S.; Griesche, J. D.; Schneller, T.; Staikov, G.; Waser, R.; Valov, I. Pr_xBa_{1-x}CoO₃ oxide electrodes for oxygen evolution reaction in alkaline solutions by chemical solution deposition. *J. Electrochem. Soc.* **2016**, *163*, F166-F170.
- (21) Zhao, B.; Zhang, L.; Zhen, D.; Yoo, S.; Ding, Y.; Chen, D.; Chen, Y.; Zhang, Q.; Doyle, B.; Xiong, X.; Liu, M. A tailored double perovskite nanofiber catalyst enables ultrafast oxygen evolution. *Nat. Commun.* **2017**, *8*, 14586.
- (22) Miao, X.; Wu, L.; Lin, Y.; Yuan, X.; Zhao, J.; Yan, W.; Zhou, S.; Shi, L. The role of oxygen vacancies in water oxidation for perovskite cobalt oxide electrocatalysts: are more better? *Chem. Commun.* **2019**, *55*, 1442-1445.
- (23) Retuerto, M.; Calle-Vallejo, F.; Pascual, L.; Lumbeeck, G.; Fernandez-Diaz, M. T.; Croft, M.; Gopalakrishnan, J.; Peña, M. A.; Hadermann, J.; Greenblatt, M.; Rojas, S. La_{1.5}Sr_{0.5}NiMn_{0.5}Ru_{0.5}O₆ double perovskite with enhanced ORR/OER bifunctional catalytic activity. *ACS Appl. Mater. Interfaces* **2019**, *11*, 21454-21464.
- (24) Sun, H.; Xu, X.; Hu, Z.; Tjeng, L. H.; Zhao, J.; Zhang, Q.; Lin, H. J.; Chen, C. T.; Chan, T. S.; Zhou, W.; Shao, Z. Boosting the oxygen evolution reaction activity

- of a perovskite through introducing multi-element synergy and building an ordered structure. *J. Mater. Chem. A* **2019**, *7*, 9924-9932.
- (25) Gunkel, F.; Christensen, D. V.; Chen, Y. Z.; Pryds, N. Oxygen vacancies: The (in)visible friend of oxide electronics. *Appl. Phys. Lett.* **2020**, *116*, 120505.
- (26) Ling, T.; Yan, D. Y.; Jiao, Y.; Wang, H.; Zheng, Y.; Zheng, X.; Mao, J.; Du, X. W.; Hu, Z.; Jaroniec, M.; Qiao, S. Z. Engineering surface atomic structure of single-crystal cobalt(II) oxide nanorods for superior electrocatalysis. *Nat. Commun.* **2016**, *7*, 12876.
- (27) Zhao, Y.; Chang, C.; Teng, F.; Zhao, Y.; Chen, G.; Shi, R.; Waterhouse, G. I. N.; Huang, W.; Zhang, T. Defect-engineered ultrathin δ-MnO₂ nanosheet arrays as bifunctional electrodes for efficient overall water splitting. *Adv. Energy Mater.* **2017**, 7, 1700005.
- (28) Lu, N.; Zhang, P.; Zhang, Q.; Qiao, R.; He, Q.; Li, H. B.; Wang, Y.; Guo, J.; Zhang, D.; Duan, Z.; Li, Z.; Wang, M.; Yang, S.; Yan, M.; Arenholz, E.; Zhou, S.; Yang, W.; Gu, L.; Nan, C. W.; Wu, J.; Tokura, Y.; Yu, P. Electric-field control of tristate phase transformation with a selective dual-ion switch. *Nature* **2017**, *546*, 124-128.
- (29) Gunkel, F.; Jin, L.; Mueller, D. N.; Hausner, C.; Bick, D. S.; Jia, C. L.; Schneller, T.; Valov, I.; Waser, R.; Dittmann, R. Ordering and phase control in epitaxial double-perovskite catalysts for the oxygen evolution reaction. *ACS Catal.* **2017**, *7*, 7029-7037.
- (30) Kim, Y. M.; He, J.; Biegalski, M. D.; Ambaye, H.; Lauter, V.; Christen, H. M.; Pantelides, S. T.; Pennycook, S. J.; Kalinin, S. V.; Borisevich, A. Y. Probing oxygen vacancy concentration and homogeneity in solid-oxide fuel-cell cathode materials on the subunit-cell level. *Nat. Mater.* **2012**, *11*, 888-894.
- (31) Biškup, N.; Salafranca, J.; Mehta, V.; Oxley, M. P.; Suzuki, Y.; Pennycook, S. J.; Pantelides, S. T.; Varela, M. Insulating ferromagnetic LaCoO_{3-δ} films: A phase induced by ordering of oxygen vacancies. *Phys. Rev. Lett.* **2014**, *112*, 087202.
- (32) Mehta, V. V.; Biskup, N.; Jenkins, C.; Arenholz, E.; Varela, M.; Suzuki, Y. Long-range ferromagnetic order in $LaCoO_{3-\delta}$ epitaxial films due to the interplay of epitaxial strain and oxygen vacancy ordering. *Phys. Rev. B* **2015**, *91*, 144418.

- (33) Lan, Q. Q.; Shen, X.; Yang, H. W.; Zhang, H. R.; Zhang, J.; Guan, X. X.; Yao, Y.; Wang, Y. G.; Yu, R. C.; Peng, Y.; Sun, J. R. Correlation between magnetism and "dark stripes" in strained La_{1-x}Sr_xCoO₃ epitaxial films ($0 \le x \le 0.1$). *Appl. Phys. Lett.* **2015**, *107*, 242404.
- (34) Gazquez, J.; Luo, W.; Oxley, M. P.; Prange, M.; Torija, M. A.; Sharma, M.; Leighton, C.; Pantelides, S. T.; Pennycook, S. J.; Varela, M. Atomic-resolution imaging of spin-state superlattices in nanopockets within cobaltite thin films. *Nano Lett.* **2011**, *11*, 973-976.
- (35) Kwon, J. H.; Choi, W. S.; Kwon, Y. K.; Jung, R.; Zuo, J. M.; Lee, H. N.; Kim, M. Nanoscale spin-state ordering in LaCoO₃ epitaxial thin films. *Chem. Mater.* **2014**, *26*, 2496-2501.
- (36) Jia, C. L.; Lentzen, M.; Urban, K. Atomic-resolution imaging of oxygen in perovskite ceramics. *Science* **2003**, *299*, 870-873.
- (37) Jia, C. L.; Urban, K. Atomic-resolution measurement of oxygen concentration in oxide materials. *Science* **2004**, *303*, 2001-2004.
- (38) Jia, C. L.; Houben, L.; Thust, A.; Barthel, J. On the benefit of the negative-spherical-aberration imaging technique for quantitative HRTEM. *Ultramicroscopy* **2010**, *110*, 500-505.
- (39) Jia, C. L.; Jin, L.; Chen, Y. H.; Urban, K. W. Wang, H. Atomic-scale evidence for displacive disorder in bismuth zinc niobate pyrochlore. *Ultramicroscopy*, **2018**, *192*, 57-68.
- (40) Ge, Z. H.; Li, W. J.; Feng, J.; Zheng, F.; Jia, C. L.; Wu, D.; Jin, L. Atomic-scale observation of off-centering rattlers in filled skutterudites. *Adv. Energy. Mater.* **2022**, *12*, 2103770.
- (41) Thust, A. High-resolution transmission electron microscopy on an absolute contrast scale. *Phys. Rev. Lett.* **2009**, *102*, 220801.
- (42) Barthel, J. Dr. Probe: A software for high-resolution STEM image simulation. *Ultramicroscopy* **2018**, *193*, 1-11.
- (43) Momma, K.; Izumi, F. VESTA 3 for three-dimensional visualization of crystal, volumetric and morphology data. *J. Appl. Cryst.* **2011**, *44*, 1272-1276.

- (44) Perdew, J. P.; Burke, K.; Ernzerhof, M. Generalized gradient approximation made simple. *Phys. Rev. Lett.* **1996**, 77, 3865-3868.
- (45) Kresse, G.; Furthmüller, J. Efficient iterative schemes for *ab initio* total-energy calculations using a plane-wave basis set. *Phys. Rev. B* **1996**, *54*, 11169-11186.
- (46) Anisimov, V. I.; Aryasetiawan, F.; Lichtenstein, A. I. First-principle calculations of the electronic structure and spectra of strongly correlated systems: the LDA+*U* method. *J. Phys.: Condens. Matter* **1997**, *9*, 767-808.
- (47) Monkhorst, H. J.; Pack, J. D. Special points for Brillouin-zone integrations. *Phys. Rev. B* **1976**, *13*, 5188-5192.
- (48) Knížek, K.; Jirák, Z.; Hejtmánek, J.; Novák, P. Character of the excited state of the Co³⁺ ion in LaCoO₃. *J. Phys.: Condens. Matter* **2006**, *18*, 3285-3297.
- (49) Pandey, S. K.; Kumar, A.; Patil, S.; Medicherla, V. R. R.; Singh, R. S.; Maiti, K.; Prabhakaran, D.; Boothroyd, A. T.; Pimpale, A. V. Investigation of the spin state of Co in LaCoO₃ at room temperature: *Ab initio* calculations and high-resolution photoemission spectroscopy of single crystals. *Phys. Rev. B* **2008**, *77*, 045123.
- (50) Togano, H.; Asai, K.; Oda, S.; Ikeno, H.; Kawaguchi, S.; Oka, K.; Wada, K.; Yagi, S.; Yamada, I. Highly active hydrogen evolution catalysis on oxygen-deficient double-perovskite oxide PrBaCo₂O_{6-δ}. *Mater. Chem. Front.* **2020**, *4*, 1519-1529.
- (51) Adler, S. B. Chemical expansivity of electrochemical ceramics. *J. Am. Ceram. Soc.* **2001**, *84*, 2117-2119.
- (52) Jia, C. L.; Barthel, J.; Gunkel, F.; Dittmann, R.; Hoffmann-Eifert, S.; Houben, L.; Lentzen, M.; Thust, A. Atomic-scale measurement of structure and chemistry of a single-unit-cell layer of LaAlO₃ embedded in SrTiO₃. *Microsc. Microanal.* **2013**, *19*, 310-318.
- (53) Jia, C. L.; Mi, S. B.; Barthel, J.; Wang, D. W.; Dunin-Borkowski, R. E.; Urban, K. W.; Thust, A. Determination of the 3D shape of a nanoscale crystal with atomic resolution from a single image. *Nat. Mater.* **2014**, *13*, 1044-1049.
- (54) Jin, L.; Barthel, J.; Jia, C. L.; Urban, K. W. Atomic resolution imaging of YAlO₃:Ce in the chromatic and spherical aberration corrected PICO electron microscope. *Ultramicroscopy* **2017**, *176*, 99-104.

(55) Aschauer, U.; Pfenninger, R.; Selbach, S. M.; Grande, T.; Spaldin, N. A. Strain-controlled oxygen vacancy formation and ordering in CaMnO₃. *Phys. Rev. B* **2013**, *88*, 054111.

Supplemental Information for

Understanding structural incorporation of oxygen vacancies in perovskite cobaltite films and potential consequences for electrocatalysis

Lei Jin,^{a†*} Feng Zhang,^{b†} Felix Gunkel,^c Xian-Kui Wei,^a Yanxing Zhang,^d Dawei Wang,^{b*} Juri Barthel,^{a,e} Rafal E. Dunin-Borkowski,^{a,f} and Chun-Lin Jia^{a,b}

- a Ernst Ruska-Centre for Microscopy and Spectroscopy with Electrons (ER-C), Forschungszentrum Jülich GmbH, 52425 Jülich, Germany.
- b School of Microelectronics and State Key Laboratory for Mechanical Behavior of Materials, Xi'an Jiaotong University, Xi'an 710049, China.
- c Peter Grünberg Institute (PGI-7), Forschungszentrum Jülich GmbH, 52425 Jülich, Germany
- d School of Physics, Henan Normal University, Xinxiang 453007, China
- e Central Facility for Electron Microscopy, RWTH Aachen University, 52074 Aachen, Germany
- f Peter Grünberg Institute (PGI-5), Forschungszentrum Jülich GmbH, 52425 Jülich, Germany
- † Equal contribution.
- * Corresponding authors. E-mail: l.jin@fz-juelich.de (L.J.) and dawei.wang@xjtu.edu.cn (D.W.)

Supplemental Table 1. Parameters used for the simulated images under negative spherical aberration imaging (NCSI) conditions, which show the best fit to the experimental images of high (Figure 4; HCM), medium (Supplemental Figure S5; MCM), and low (Supplemental Figure S6; LCM) contrast modulation areas. The semi-convergent angle and the focus spread were set to 0.3 mrad and 3 nm for all simulations, respectively.

	HCM area	MCM area	LCM area
Parameters	Magnitude		
Specimen thickness	4.4 nm	4.4 nm	4.8 nm
Specimen tilt	(0.0, 1.9) mrad	(-0.3, 2.1) mrad	(1.2, -2.3) mrad
Absorption	0.018	0.018	0.018
Image spread	20 pm	20 pm	26 pm
Overfocus C_1	3.56 nm	3.76 nm	2.85 nm
Two-fold astigmatism A_1	(0.1, 0.4) nm	(-1.2, 0.1) nm	(0.0, -0.3) nm
Three-fold astigmatism A_2	(-35, -34) nm	(93, 27) nm	(17, 12) nm
Coma B_2	(-18, -16) nm	(-24, -68) nm	(-19, -95) nm
3^{rd} -order spherical aberration C_3	-13 μm	-13 μm	-14 μm
5 th -order spherical aberration C_5	4 mm	4 mm	4 mm
$B_{ m Pr,Ba}$	0.0053 nm^2		
B_{Co}	$0.0021 \; nm^2$		
$B_{\mathrm{O}(1)}$	$0.0052 \; \mathrm{nm^2}$		
$B_{\mathrm{O}(2)}$	$0.0055 \; \mathrm{nm^2}$		

Note: Parameters of specimen tilt, A_1 , A_2 and B_2 are given in the format of (horizontal component, vertical component). Isotropic B parameters for Debye-Waller factors were taken from ICSD 164818 for room temperature $PrCoO_3$, as no existing data for $Pr_{0.5}Ba_{0.5}CoO_3$ was found in literature.

Supplemental Note 1:

We note, in Figure 4a the oxygen columns exhibit an elongated shape, which are still not perfectly reproduced by the simulation as shown in Figure 4b. We consider the possible reasons as follows:

- i) In the raw image Figure 3a, individual oxygen columns at the same Co-O plane show position variations in the [001] direction (elongation direction), inevitably resulting in the apparent (vertical) elongation of oxygen columns in the averaged image Figure 4a;
- ii) The incorporation of oxygen vacancies may induce oxygen octahedral distortion, as suggested by our density functional theory (DFT) calculations (not shown), leading to slight relative shifts of individual oxygen atoms in an atomic column. Such a distortion, *i.e.*, oxygen atoms do not line up along the viewing direction, was not included in our simplified model used in Figure 4c.

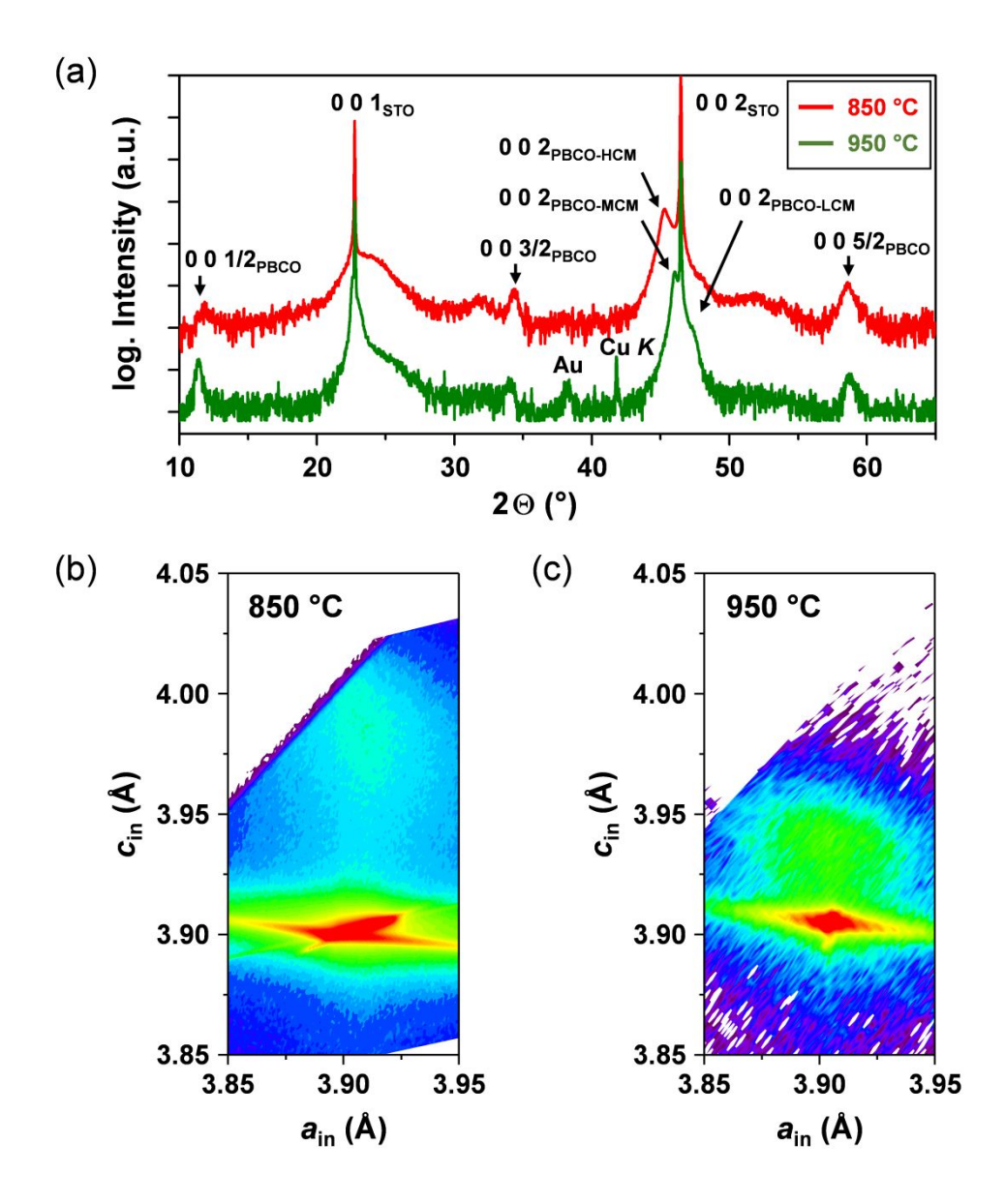


Figure S1 (a) X-ray diffraction (XRD) results showing the phase structure of the PBCO films. Superstructural diffraction peaks are labeled by $(0\ 0\ l/2)_{PBCO}\ (l=\text{odd})$. The peaks located at the lower- and higher-angle shoulders in the vicinity of the substrate peak originate from the medium contrast modulation (MCM) and low contrast modulation (LCM) areas of PBCO grown at 950 °C (see Figure 1b in the main text), respectively, revealing the structural inhomogeneity. The peaks labeled by Au and Cu K

originate from the gold layer (deposited for focused ion beam preparation) and the X-ray source. (b) and (c) Reciprocal space map information around the SrTiO₃ (013) reflection showing the presence of in-plane lattice strain for both films.

The following issues must be emphasized:

- i) Owing to the kinematic scattering nature of XRD, the intensity of the superstructural peaks is actually dominated by the contribution of lattice/distance modulation of Pr/Ba-Pr/Ba atoms, although the modulation itself is associated with oxygen vacancy ordering. This leads to intrinsic difficulties in verifying phase structures using XRD refinement in the present case.
- ii) The intensity of superstructural peaks are also influenced by the presence of Ruddlesden-Popper (R-P) ordering, particularly for the sample grown at 850 °C.
- ii) The presence of superstructural peaks in XRD is *not* a unique criterion in distinguishing Pr/Ba cation ordered double perovskites from oxygen vacancy ordered single perovskites.

Supplemental Table 2. Out-of-plane structural parameter c derived from XRD, high-resolution scanning transmission electron microscopy (STEM) and NCSI, respectively. It should be noted that XRD represents the averaged information, while transmission electron microscopy (TEM) shows localized structure. It can be seen that within the measurement error (< 8 pm for both STEM and NCSI), the results are consistent with each other.

	XRD	STEM	NCSI
РВСО-НСМ	002 _{PBCO-HCM} : Sharp peak at ~45.3°		$c_{\text{low}} + c_{\text{high}} = 7.963 \text{ Å}$
	$\rightarrow c \approx 4.001 \text{ Å}$	c = 3.967 Å	$\rightarrow c = 3.982 \text{ Å}$
	Supplemental Figure S1	Figure 2a,b	Figure 4
PBCO-MCM	$002_{\text{PBCO-MCM}}$: Sharp peak at ~46° $\rightarrow c \approx 3.943 \text{ Å}$ Supplemental Figure S1	c = 3.965 Å Figure 2c,d	$c_{\text{low}} + c_{\text{high}} = 7.983 \text{ Å}$
	$002_{PBCO-LCM}$: Broad shoulder at ~47.5°		$c_{\text{low}} + c_{\text{high}} = 7.750 \text{ Å}$
PBCO-LCM	$\rightarrow c \approx 3.826 \text{ Å}$		$\rightarrow c = 3.875 \text{ Å}$
	Supplemental		Supplemental
	Figure S1		Figure S6

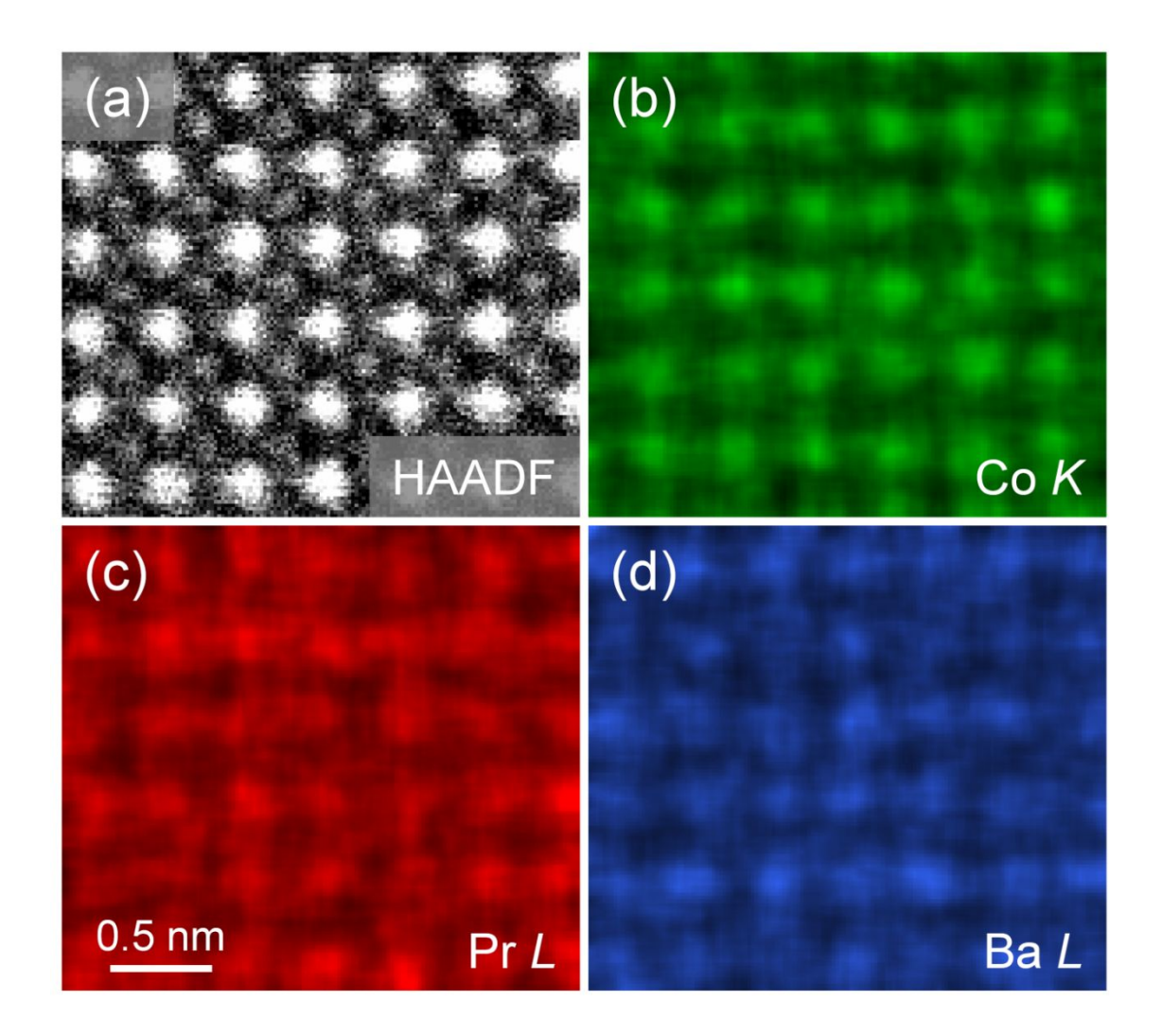


Figure S2 Atomic-resolution high-angle annular dark-field image and corresponding energy dispersive x-ray spectroscopic (EDXS) maps of Co K, Pr L and Ba L lines, respectively, providing evidence for the absence of A-site atomic ordering. The measured cationic ratio is $Pr_{0.51}Ba_{0.49}Co_{0.95}$. We note the error of EDXS measurement is typically on the order of 5% to 10%, for this we conclude that there is no significant deviation from the nominal value. Further measurements from different local areas show similar values for both 850 and 950 °C grown samples, suggesting that the influence of cation nonstoichiometry on the lattice expansion is minor.

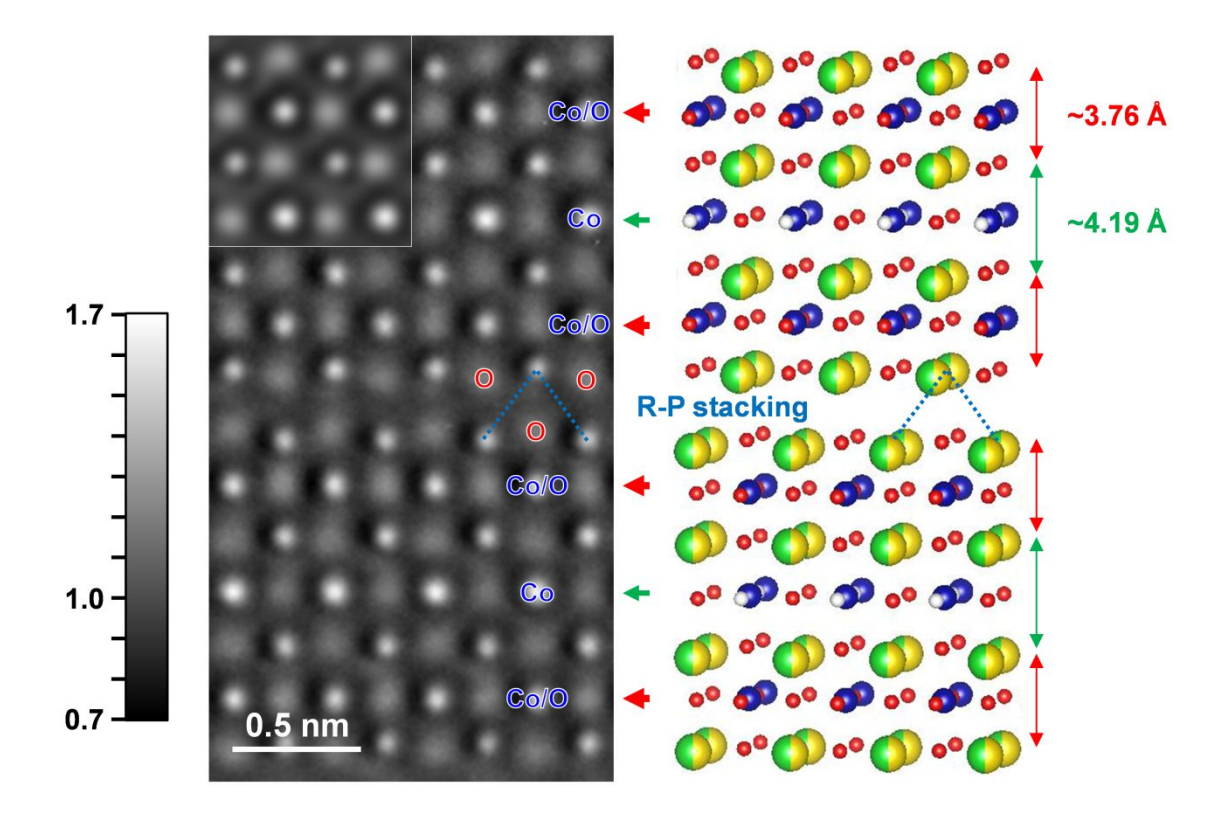


Figure S3 (Left) Negative spherical aberration image taken from the [100] direction of the sample grown at 850 °C. Inset is the best-fit simulated image. (Right) Atomic model used for the image simulation. Pr/Ba: yellow/green; Co: blue; O: red; O_{vacancy}: white. The O_{high} and O_{low} planes are marked by red and green arrows, respectively. In this viewing direction, the oxygen vacancies are ordered in the columns including Co atoms (indicated by Co) in the O_{low} planes, which leads to enhanced column intensities as compared to those columns with fully-occupied O and Co atoms (indicated by Co/O). A local Ruddlesden-Popper (R-P) stacking fault is revealed, mediated by the relative half-perovskite-unit-cell shift between the top and bottom variants.

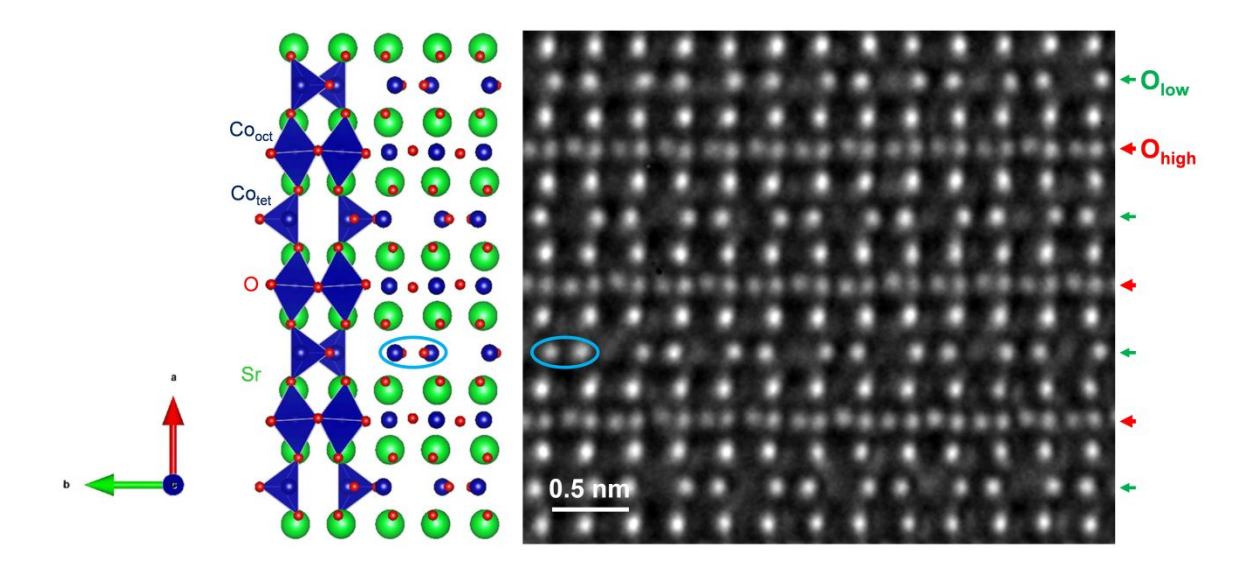


Figure S4 (Left) Atomic model of $SrCoO_{2.5}$ (ICSD 162241), a typical brownmillerite structure, projected along the pseudocubic perovskite [110] direction, showing the structural response to the presence of ordered oxygen vacancies ($\delta = 0.5$). At the oxygen deficient Co-O plane (*i.e.*, O_{low}), the Co atoms are in an oxygen tetrahedral coordination environment (denote Co_{tet}), forming a pair structure marked by blue ellipses in comparison with those located in oxygen octahedra (denote Co_{oct}). (Right) Atomic-resolution image of $SrCoO_{2.5}$ recorded under NCSI conditions, showing the structural changes at Co_{tet} columns. This is clearly different from that shown in Figure 3 in the main text.

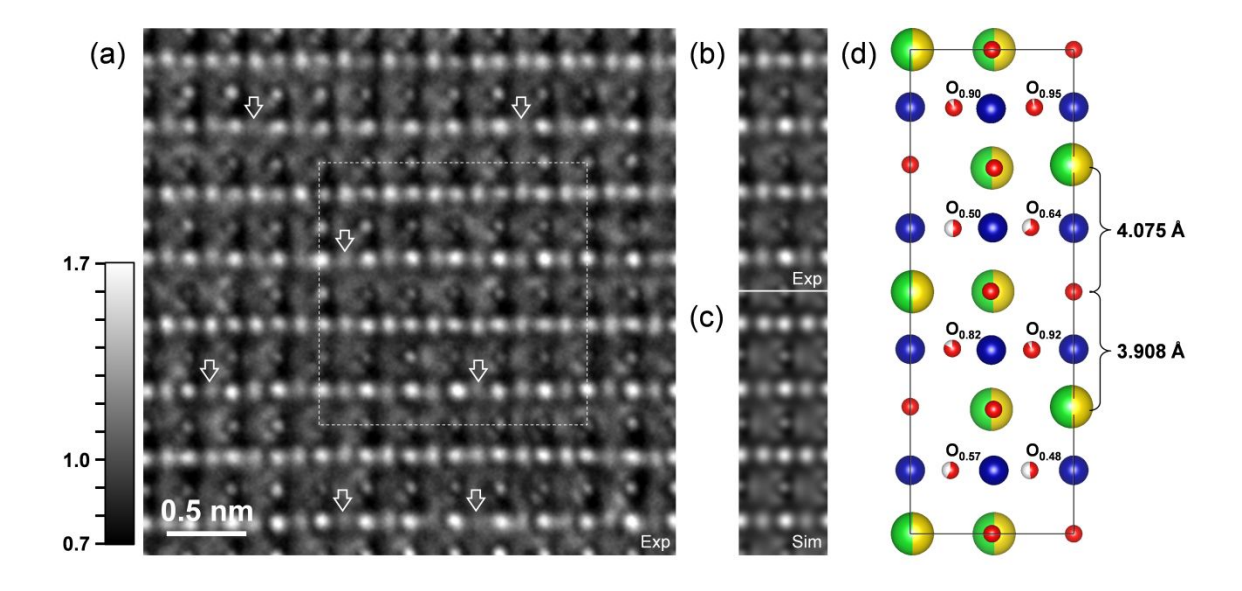


Figure S5 (a) Atomic-resolution TEM image recorded under NCSI conditions along the pseudocubic [110] direction, showing the intensity variations of O columns (*e.g.*, see columns marked by open arrows) in a medium contrast modulation region (see Figure 1b in the main text) of the 950 °C grown sample. (b) Experimental image averaged over the marked area in (a). (c) The best-fit simulated image using the atomic model shown in (d). The parameters for image simulation are listed in the Supplemental Table S1. The stacking sequence along the pseudocubic [001] can be described as ...- $Pr_{0.5}Ba_{0.5}O$ - $CoO_{2\times0.55}$ - $Pr_{0.5}Ba_{0.5}O$ - $CoO_{2\times0.9}$ -... (*i.e.*, $Pr_{0.5}Ba_{0.5}CoO_{2.45}$) and lattice distance of $c_{high} + c_{low} = 4.075 + 3.908 = 7.983 Å.$

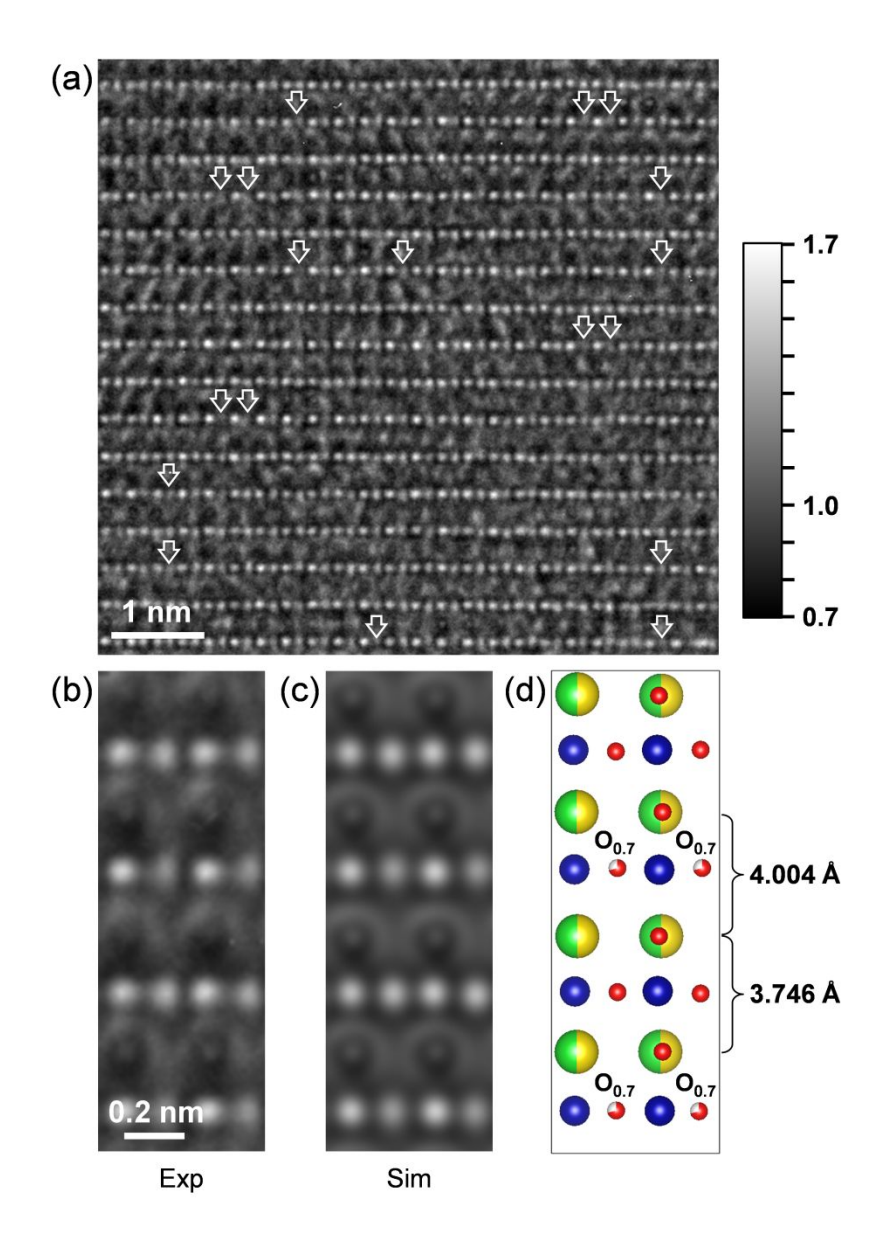


Figure S6 (a) Atomic-resolution TEM image recorded under NCSI conditions along the pseudocubic [110] direction, showing the intensity variations of O columns (*e.g.*, see columns marked by open arrows) in a low contrast modulation region (see Figure 1b in the main text) of the 950 °C grown sample. (b) Averaged experimental image and (c) the best-fit simulated image using the atomic model shown in (d). The parameters for image simulation are listed in the Supplemental Table S1. The stacking sequence along the pseudocubic [001] can be described as ...- $Pr_{0.5}Ba_{0.5}O-CoO_{2\times0.7}-Pr_{0.5}Ba_{0.5}O-CoO_{2}-...$ (*i.e.*, $Pr_{0.5}Ba_{0.5}CoO_{2.7}$) and lattice distance of $c_{high} + c_{low} = 4.004 + 3.746 = 7.750 Å.$

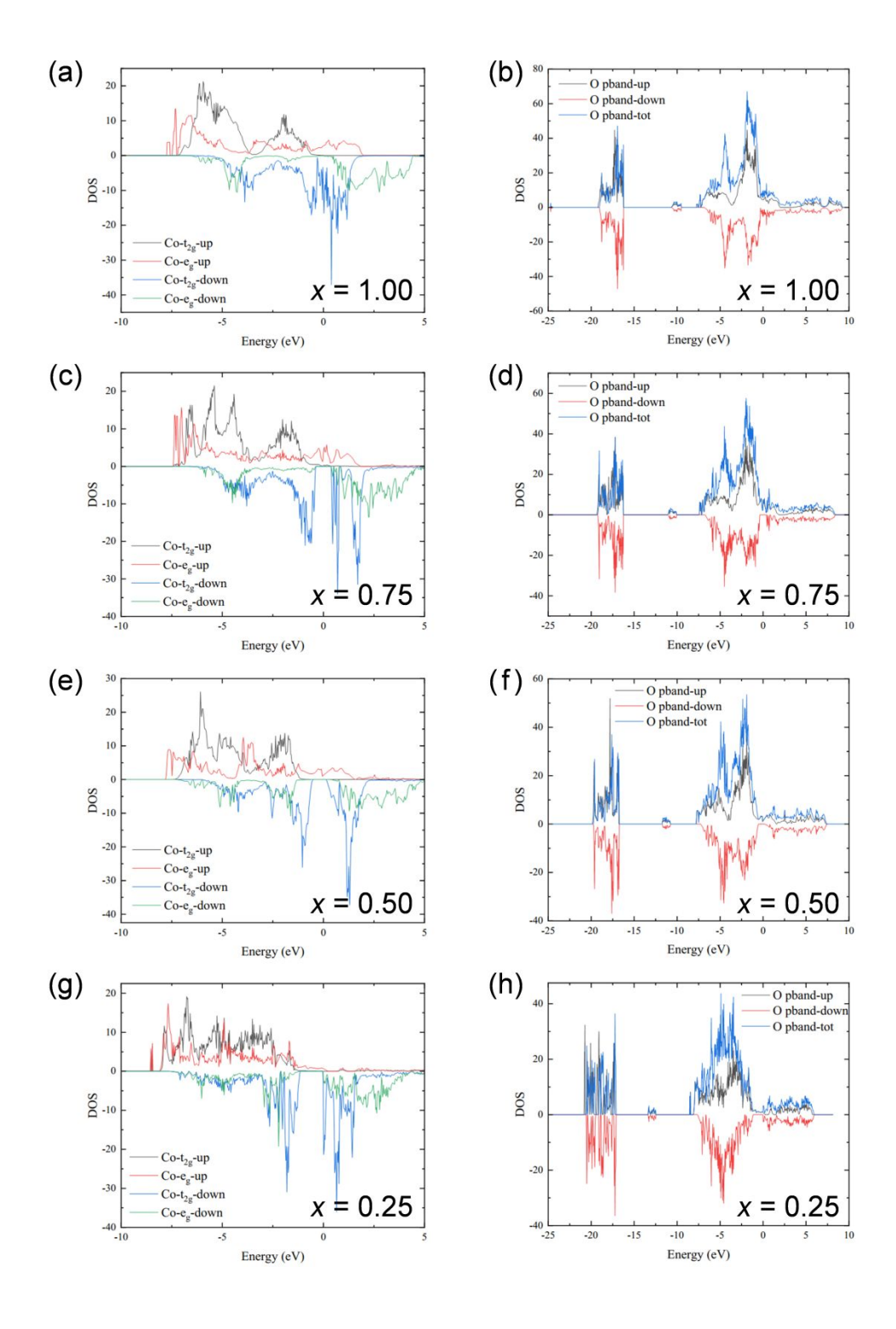


Figure S7 Density-of-states (DOS) of Co 3d orbitals and O p-bands calculated from first-principles density functional theory for different O occupancies at CoO_{2x} planes. (a,b) x = 1.00, (c,d) x = 0.75, (e,f) x = 0.50 and (g,h) x = 0.25.